Research Square

Preprints are preliminary reports that have not undergone peer review.
They should not be considered conclusive, used to inform clinical practice,
or referenced by the media as validated information.

Hybrid Optimization Method for Additively Manufactured Permanent Magnet Synchronous Motors

Hager Salem
Mansoura University
Maged Ibrahim
maged.ibrahim@giu-uni.de
German International University of Cairo
Eid Gouda
Mansoura University
Maniya Aghasibeig
National Research Council Canada
Jean-Michel Lamarre
National Research Council Canada
Fabrice Bernier
National Research Council Canada

Article

Keywords: Interior permanent magnet synchronous motor (IPMSM), Genetic algorithm (GA), Normalized Gaussian network (NGnet), Parameter optimization (PO), Topology optimization (TO), Additive manufacturing (AM).

Posted Date: February 27th, 2026

DOI: https://doi.org/10.21203/rs.3.rs-8892847/v1

License: This work is licensed under a Creative Commons Attribution 4.0 International License.
Read Full License

Additional Declarations: No competing interests reported.

Hybrid Optimization Method for Additively Manufactured Permanent Magnet Synchronous Motors

Hager Salem[1,2], Maged Ibrahim[2*], Eid Gouda[1], Maniya Aghasibeig[3], Jean-Michel Lamarre[3] and Fabrice Bernier[3]

[1]Electrical Engineering Department, Faculty of Engineering, Mansoura University, Mansoura 35516, Egypt
[2]German International University of Cairo, Administrative Capital, Regional Ring Rd, Cairo Governorate Desert, Cairo, Egypt
[3]National Research Council Canada, Automotive Research Center, Boucherville, Québec, J4B6Y4, Canada
maged.ibrahim@giu-uni.de

ABSTRACT

This paper presents a new two-step optimization process for the rotor of a multilayer Interior Permanent Magnet Synchronous Motor (IPMSM), using additive manufacturing (AM) to create a layered rotor made from alternating soft magnetic materials (SMM) and permanent magnet (PM) layers. The process starts with parametric optimization (PO), to determine the optimum number and dimensions of the PM layers, leading to a solid baseline design. The second step was topology optimization (TO), using the NGnet method to achieve the optimum rotor geometry, mainly to reduce demagnetization risk. The TO was run using different mesh element sizes to investigate the mesh refinement effect on the design. The final rotor design that was optimized is characterized by a higher torque density, improved use of PM material, and a lower risk of demagnetization when compared to the baseline design. The optimization process presented in this paper provides a valuable approach for the design of high performance IPMSM rotors and subsequent manufacture through additive manufacturing.

Keywords

Interior permanent magnet synchronous motor (IPMSM), Genetic algorithm (GA), Normalized Gaussian network (NGnet), Parameter optimization (PO), Topology optimization (TO), Additive manufacturing (AM).

Abbreviations

IPMSMs	Interior permanent magnet synchronous motors
AM	Additive manufacturing
PMs	Permanent Magnets
SMMs	Soft Magnetic Materials
CSAM	Cold Spray Additive Manufacturing
IPM	Interior Permanent Magnet
wt.%	weight percent
AC	Alternating Current
DC	Direct current
FEA	Finite element analyses
PO	Parametric Optimization
MOGA	Multi-Objective Genetic Algorithm
GD	Goodness factor
TO	Topology optimization
NGnet	Normalized Gaussian network
FE	Finite element

List of symbols

L_q	Quadrature-axis inductance, H
L_d	Direct-axis inductance, H
W_i (i= 1-3)	Radial thickness of the *i*-th PM layer, mm

α_i	Angle of the *i*-th SMM layer at the rotor surface, °
β_i	Angle of the *i*-th PM layer at the rotor surface, °
γ	Current phase angle, °
N_{var}	Total number of optimization variables in parametric optimization
N_{lay}	Number of rotor layers
T_{emg}	Electromagnetic torque, Nm
P_{loss}	Total motor losses, W
B_r	Remanent magnetic flux density (remanence), T
H_c	Coercive field strength (coercivity), A/m
$y(x)$	Shape (material distribution) function
G_i	*i*-th Gaussian basis function
b_i	Normalized *i*-th Gaussian basis function
N	Total number of Gaussian basis functions
w_i	weighting coefficient of the *i*-th Gaussian function
$\boldsymbol{w}$	vector of weighting coefficients
$\boldsymbol{x}$	position vector in the design domain
σ	standard deviation of the Gaussian basis function

Introduction

There is a growing demand for electric motors with high power density and efficiency to meet the performance requirements of modern electrified transportation systems. As performance demands increase, optimizing motor geometries is of particular interest to research efforts in order to improve torque and efficiency, and to reduce losses and expensive magnet materials. Many different machines exist but interior permanent magnet synchronous motors (IPMSMs) are widely used in a variety of applications for their high efficiency and torque performance, compact design, and relatively constant power across a wide range of speeds[1,2]. However, Conventional laminated IPMSMs have a several design limitations due to manufacturing, which restrict the electromagnetic performance. The flux barrier geometry has to be simplified (e.g., either trapezoidal or triangular) due to punching and stacking limitations, preventing the use of theoretically optimal shapes, which could improve torque generation and reduce ripple[3]. In laminated rotors, bridges and center posts must be added to withstand centrifugal stresses at high speeds. However, these elements create low-reluctance leakage paths, hence reducing the saliency and torque capability[4]. Layered IPMSMs, made possible with Additive Manufacturing (AM), overcome these limitations by eliminating mechanical center posts and bridges through sequential layers of Permanent Magnets (PMs) and Soft Magnetic Materials (SMMs). The design offers greater saliency ratios ($L_q/L_d \approx 10$), lower leakage flux, and greater flux-weakening ability, resulting in improved torque density and reduced magnet usage compared to conventional IPMSMs with laminated rotors[5,6]. In electric machine applications, AM has the potential to outperform traditional techniques such as lamination, punching and stacking, since this technology can create complicated stator and rotor geometries, custom winding patterns, and even embed thermal management structures, all of which can increase torque density and improve electric machine efficiency and cooling performance[7,8].

Various components of electric machines, including PMs, windings, and soft magnetic cores, can now be fabricated using a range of AM techniques. These techniques, which include cold spray, fused filament fabrication, and laser sintering, enable nearly net-shape manufacturing processes that reduce material consumption and post-machining needs[9,10]. This study applied Cold Spray Additive Manufacturing (CSAM), a solid-state process that creates dense components without melting by accelerating metallic powders to supersonic velocities. CSAM is particularly useful because it can minimize oxidation, thermal stresses, and microstructural degradation and can be used to fabricate layered rotor structures and dense magnetic components[11]. CSAM therefore opens the door to new motor architectures that combine performance improvement with manufacturing flexibility.

Geometry optimization of electric machines play a crucial role in enhancing the machine performance. Two widely-used methods are as follows: the first method is parametric optimization (PO), in which selected parameters can be changed effectively within predefined ranges[12-14], the second method is topology optimization (TO), in which there is more freedom for redistributing material geometries[15-17]. While TO can produce very effective and complex motor geometries, such geometries are difficult to fabricate through conventional manufacturing methods.

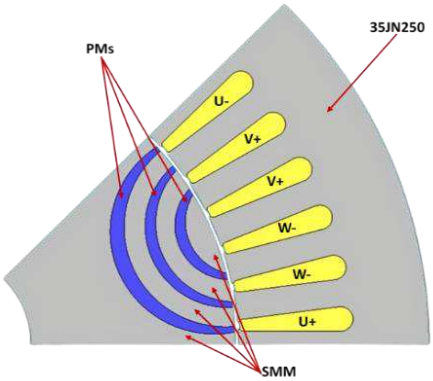


Fig. 1. Cross-sectional view of the layered IPMSM

This issue is resolved using AM to produce complicated, non-conventional geometries from topology-optimized models[9,10]. Hybrid implementation of Parametric-topology optimization of layered IPMSMs tailored using AM have been the subject of very few studies. A hybrid method that leverages the swift convergence of PO and the design freedom of TO, with considerations for AM, is needed to create high-performance, manufacturable motor geometries, closing a fundamental research gap in the design of advanced electric machines.

This paper introduces a hybrid parametric–topology optimization strategy for the rotor of layered IPMSM fabricated by CSAM. The paper is arranged as follows; section 2 provides the detailed description of the layered motor structure. The parametric optimization method for optimizing the motor's main design parameters is explained in section 3. The topology optimization process for achieving additional performance enhancements is described in section 4.

Layered Motor Description

The motor under investigation is an Interior Permanent Magnet (IPM) motor that has a rotor made of alternating layers of isotropic NdFeB permanent magnets and soft magnetic material (SMM), as shown in Fig.1. This construction removes mechanical bridges and center-posts inherent to traditional IPM rotors, reducing flux leakage and enhancing the saliency ratio while maintaining sufficient structural integrity for high-speed operation[6]. The baseline rotor contains three layers of NdFeB magnets alternated with SMM segments. The rotor's hard and soft magnetic layers were produced via CSAM, a solid-state process that accelerates powders to supersonic velocities, bonding them without melting[18-19]. This allows retention of intrinsic powder magnetic properties while creating dense deposits with excellent mechanical strength.

In the case of the hard magnetic NdFeB layers, the material was fabricated from a composite containing 90 wt.% MQFP-B NdFeB powder and 10 wt.% fine aluminium binder (H3, D50 ≈ 4 µm), sprayed at gas temperatures between 600 and 700 °C and at 4.9 MPa[18]. This composition and fine binder size maximized magnetic phase loading and minimized binder dilution. The resulting deposits exhibited magnetic remanence up to 0.49 T at a magnetic volume fraction of 68%, which is lower than the approximately 1.4 T typical of sintered NdFeB magnets due to the use of isotropic powder and the presence of binder. The intrinsic coercivity was in the range of 693–715 kA/m, very close to feedstock powder values, showing minimal thermal degradation during spraying. The energy product was measured at around 36 kJ/m³. Mechanically, these cold-sprayed magnets achieved an ultimate tensile strength of roughly 200 MPa, considerably higher than bonded or polymer-based magnets because of the metallic binder and the high degree of particle deformation during deposition. The microstructure was dense and low in porosity, with the magnetic phase uniformly distributed within the aluminium matrix. While the high mechanical integrity makes them well suited for high-speed rotor operation and enables fabrication of complex shapes without assembly, the reduced Br compared to sintered magnets and the higher electrical conductivity from the aluminium binder (about 12 MS/m) can lead to increased eddy current losses unless mitigated in the motor design.

For the SSM layers, the highest-performing composition was obtained using a cold spray premix of 24% pure iron and 76% Fe3.8Si alloy. This blend was selected for its higher electrical resistivity compared to pure iron, which helps reduce eddy current losses, while maintaining good magnetic performance. The deposits achieved a density of approximately 7.40 g/cm³, a permeability of about 360, and a B12000 of 1.61 T. Although the permeability is lower than that of pure Fe, the significantly higher resistivity of Fe3.8Si makes this composition more suitable for reducing AC losses. To further improve DC performance, a post-deposition heat treatment at 480 °C for 20 minutes increased permeability by 44% (to around 520) and reduced coercivity by 22%, indicating lower hysteresis losses. However, this treatment also increased total AC losses by

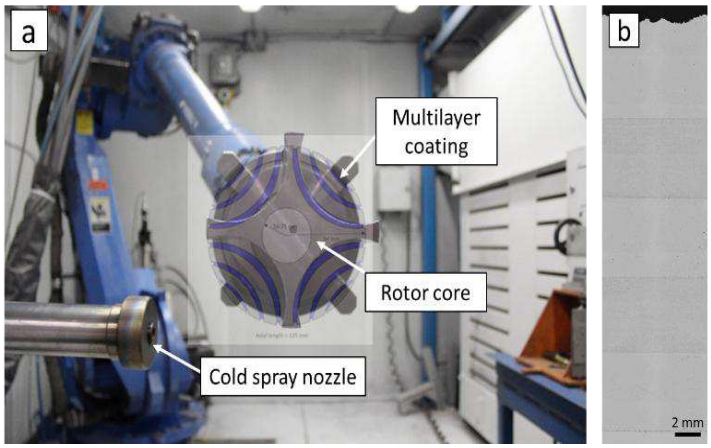


Fig. 2. a) CSAM setup for the deposition of the multilayer motor on a 4-pole rotor core, and **b)** five-layer CSAM SMM-NdFeB composite buildup with layer thickness of ≥ 5mm, and total thickness of > 25

Parameter	Unit	Value
Stator outer diameter	mm	264
Stator inner diameter	mm	161.9
Air gap length	mm	0.75
Stack length	mm	50.8
Number of phases		3
Number of poles		8
Number of slots		48
Rotor core material		Fe_Fe3.8Si
Rotor magnet material		NdFeB (MQFP-B grade, Br = 0.49 T)
Lamination material		35JN250

Table 1. Specifications of the layered IPMSM.

roughly 10% at 60 Hz and 18% at 400 Hz. The resulting combination of mechanical robustness, improved resistivity, and acceptable permeability makes the 24%Fe–76%Fe3.8Si composition the most balanced choice for the layered IPMSM rotor's soft magnetic segments.

The CSAM strategy developed for fabricating the layered IPMSM motor involves mounting a 4-pole mild-steel rotor core on a 6-axis industrial robot capable of rapid and precise 3D movements (Fig. 2-a). The spray nozzle is programmed to traverse along the rotor's longitudinal axis during deposition, with dynamic adjustments to the standoff distance to account for the curved rotor pole geometry. After deposition of each layer, the rotor surface is machined to the target thickness and geometry before resuming cold spray for the subsequent layer. This alternating deposition-machining sequence is repeated until the final rotor geometry, comprising alternating SMM and NdFeB layers, are achieved. Fabricating thick multi-material layers for the multilayer rotor using cold spray presents several challenges that directly affect mechanical integrity and, consequently, the rotor's ability to operate at high speeds. Achieving the required strength requires excellent cohesion and adhesion of the buildup layers, while maintaining precise control over thermal and residual stresses generated during deposition. These challenges are further complicated by mismatches in material properties between the permanent magnet and soft magnetic layers. Insufficient mechanical integrity in such a structure would limit the maximum safe operating speed and compromise overall motor performance. To address these challenges, the CSAM fabrication strategy incorporated optimized heat treatments tailored to the multilayer buildup to enhance the overall material strength and structural integrity. Following this approach, a five-layer deposit, with each layer approximately 5 mm thick, was successfully built on a mild-steel substrate (Fig. 2-b), resulting in a rotor structure with the mechanical robustness needed for high-speed operation while maintaining the desired magnetic characteristics.

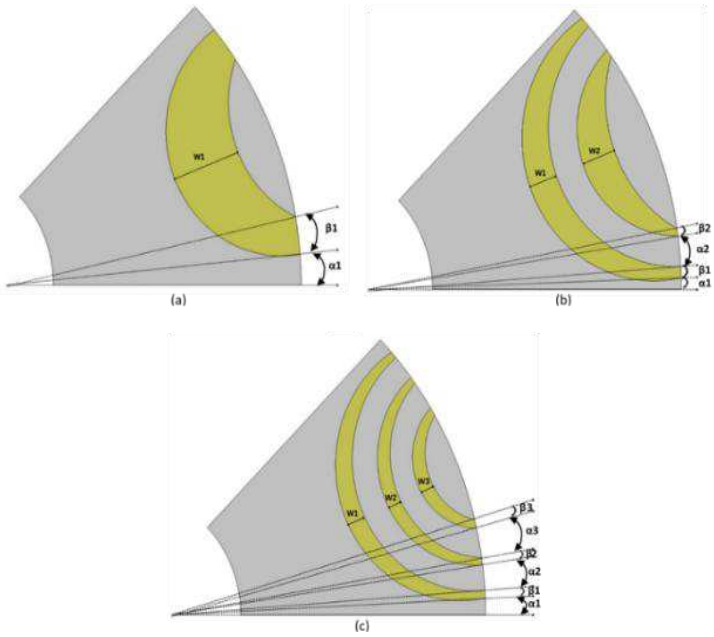


Fig. 3. Initial rotor design for (a) 1 layer, (b) 2 layer, (c) 3 layer.

Variable	Range		
	1layer	2layer	3layer
W_1 [mm]	0.3 to 19.3	6 to 15.6	4 to 13
W_2 [mm]	-	3 to 8.8	3 to 11
W_3 [mm]	-	-	2.8 to 7
α_1 [degree]	0.6 to 14.7	0.5 to 3	1 to 7
α_2 [degree]	-	0.5 to 7.7	1 to 9
α_3 [degree]	-	-	1 to 7
β_1 [degree]	0.2 to 16	0.9 to 5	0.9 to 8
β_2 [degree]	-	0.5 to 7	0.8 to 7
β_3 [degree]	-	-	0.7 to 6
γ [degree]	0 to 90		

Table 2. Range of the selected design variables

All electromagnetic finite element analyses (FEA) in this study were performed using JMAG software[20]. Table 1 shows key specifications of the initial layered motor design.

Parametric Optimization

The proposed optimization process begins with a Parametric Optimization (PO) performed by a Multi-Objective Genetic Algorithm (MOGA). The purpose of this step is to determine the optimal number of PM layers and the associated rotor geometric parameters that achieve the best trade-off between performance and material usage. In this section, the MOGA process, optimization objectives, design constraints, and variable ranges are described.

Implementation of MOGA on Layered IPMSM

In this section, three rotor configurations with one, two and three layers of PMs will be investigated. As layer count increases the complexity of the rotor structure also increases which places a practical burden on manufacturing. In addition, increasing the number of layers also increases the number of design variables which increases the search space and computational time, thus only configurations up to three PM layers were investigated.

The range of the selected design variables for optimization is shown in Table 2, with corresponding configurations illustrated in Fig. 3. For each rotor configuration, W_1 to W_3 represent the radial thickness of the PM layers, The angles α_1 to α_3 define the angles of the SMM layers at the rotor surface, while β_1 to β_3 define the angles of the PM layers at the rotor

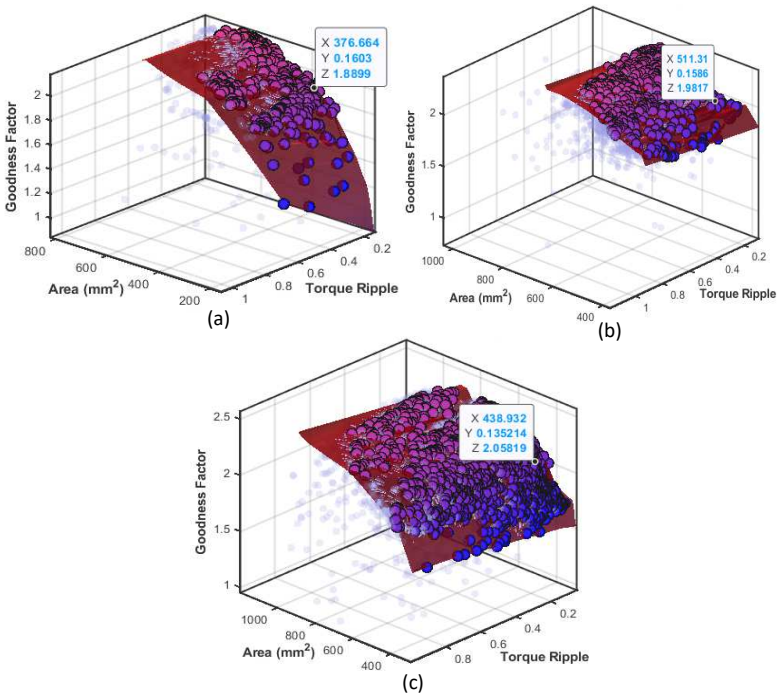


Fig. 4. 3D pareto front with optimal design point for (a) 1-layer, (b) 2-layer, (c) 3-layer configuration.

surface. The current phase angle γ is also included as an optimization variable. The total number of variables to be optimized is then $N_{var} = 3N_{lay}+1$, where N_{lay} is the number of rotor layers.

The phase current amplitude was held constant at 170 Arms during the optimization. The objectives of optimization are:

- Maximize the machine goodness factor (GD) — to enhance the overall motor performance based on torque output, and total losses. The GD was first defined in[21] as a methodology to evaluate motor performance based on shaft torque. In the present study the GD is based on the electromagnetic torque consistent with previous studies[22,23]. The machine goodness GD is expressed as:

$$\mathrm{GD} = \frac{\mathrm{T_{emg}}}{\sqrt{\mathrm{P_{loss}}}} \qquad (1)$$

  where T_{emg} is the electromagnetic torque and P_{loss} represents the total motor losses. The total losses in the motor consist of Copper losses, Iron losses, and PM losses.
- Minimize torque ripple.
- Minimize the magnet area that directly results in decreasing total cost, and rare-earth material dependence.

The optimization is subject to the following constraints:

- The electromagnetic average torque must be greater than or equal 200 N.m.
- Power factor must be greater than or equal 0.5.

Analysis of Optimization Results

The 3D Pareto fronts for the optimized 1-, 2-, and 3-layer rotor configurations are presented in Fig. 4. In each plot, the Pareto surfaces represent the trade-off region of optimal solutions, demonstrating the compromise relationships between high machine GD, low torque ripple, and reduced magnet area. In multi-objective optimization, it's often that no one design meets all of the objectives at the same time. Instead, a compromise must be made in the final choice.

For each configuration, the optimal design was selected from the Pareto front based on the boundary constraints. The cross-sections of these selected designs are shown in Fig. 5.

The key performance factors of the optimal design for each rotor configuration are listed in Table 3, along with the initial design. The parametrically optimized 3-layer configuration possesses the best compromise between our objectives of all configurations. Compared to the baseline design, the proposed 3-layer optimal design achieves an average torque

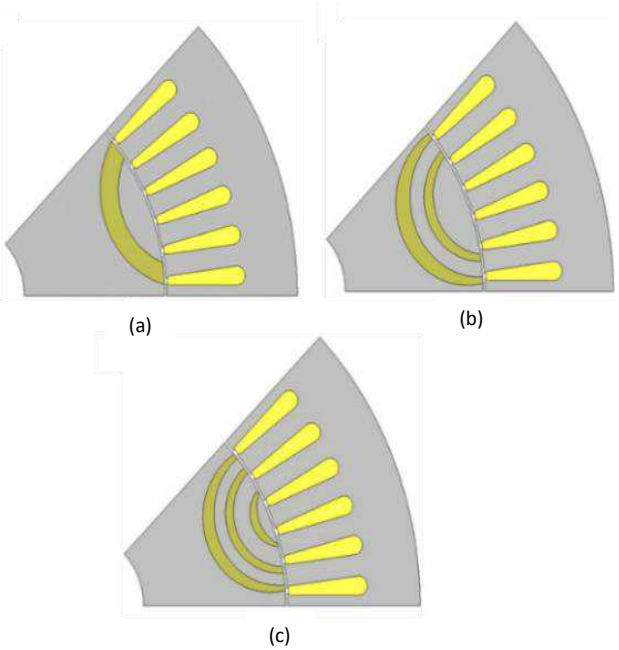


Fig.5. Cross section of the optimal design for each configuration: (a) 1- layer, (b) 2- layer, (c) 3- layer.

Performance Metric	1 Layer optimal design	2 Layer optimal design	3 Layer	
			Optimal design	Initial design
Average Torque [Nm]	204.906	216.403	228.85	226.8
Torque ripple percentage	16.03%	15.86%	13.52%	21.86%
Magnet Area [mm^2]	376.664	511.31	438.93	453.75
Goodness Factor (GD)	1.8899	1.9817	2.0582	2.04
Power Factor	0.5107	0.5314	0.5505	0.544
Total Losses at 200 Nm [W]	11031.9	9777.7	8709.2	8942.6

Table3. Comparison of Initial Design and Optimal Rotor Designs

increase of approximately 0.9%, a torque ripple reduction of about 38.2%, a magnet area reduction of around 3.3%, an improvement of the GD by about 0.9%, a power factor increases by 1.2%, and a decrease in total losses at 200 Nm by about 2.6%, validating the advantage of the PO approach. To better understand the trend in performance between configurations, 2D projection plots of the 3D Pareto surfaces are provided in Fig. 6. In GD vs magnet area and GD vs torque ripple plots, the 3-layer configuration consistently outperforms in terms of trade-offs. With the same values for GD, it produces less torque ripple and smaller magnet area than 1- and 2-layer solutions, confirming its supremacy in objectives. Moreover, the 3-layer Pareto front continues to extend further towards higher GD values with minimum magnet area and torque ripple, yielding solutions that push the performance boundary beyond what is possible through the other configurations.

This output advantage is due to the increased rotor saliency caused by the additional PM layers. As the number of magnet layers increases, the rotor saliency improves greatly, and the contribution of reluctance torque is enhanced. Hence, high total output torque is achieved with an imposed decrease in PM torque contribution[24].

Based on the MOGA optimization results and the comparison study with the 1- and 2-layer structures, as well as the initial design, the optimized 3-layer rotor is selected as the final optimum solution. The final optimum design satisfies all performance constraints and is the best overall compromise between objectives.

PM Demagnetization

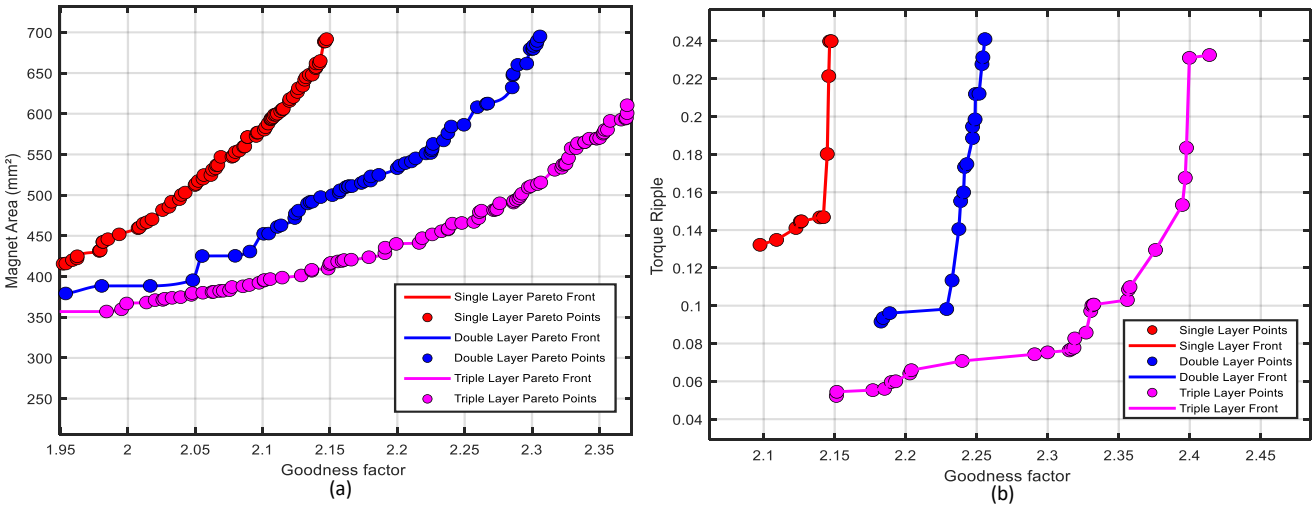


Fig.6. Projected 2D Pareto fronts comparing 1-, 2-, and 3-layer configurations: (a) GD vs. Torque Ripple, (b) GD vs. Magnet Area.

A demagnetization analysis is performed since the PM material used is additively manufactured isotropic NdFeB. Unlike conventional sintered magnets, AM-based magnets—particularly those fabricated via cold spray processes—tend to exhibit lower magnetic properties, especially in terms of remanence (B_r) and coercivity (H_c).

In our study, the use of MQFP-B isotropic NdFeB powder requires careful evaluation of demagnetization risk under motor operating conditions. As noted by Bernier et al.[25], magnets produced using AM processes tend to underperform the sintered magnets. This reduced magnetic performance can be attributed to several factors, including the use of non-magnetic binders in certain AM techniques, which lowers the overall magnetic phase content, and the inherent limitations of isotropic powders, which lack grain alignment—since robust methods for aligning anisotropic powders during AM are still under development.

Demagnetization analysis was performed on the optimum 3-layer rotor structure for two operating states. For the initial condition, the rotor was loaded at its maximum armature current with its current phase angle set to pure demagnetizing d-axis direction, which is the worst-case magnetic load state. In the second case, the same armature current magnitude was employed but with the normal operating current phase angle to find the effect of the armature reaction field on the PMs under normal operation. Following the current application to both cases, the machine was subjected to no-load operation, and the demagnetization level was obtained from the armature flux linkage reduction. The demagnetization analysis in this research is done using the magnet demagnetization properties at 25˚C. The demagnetization ratios distributions for both cases are presented in Fig. 7. These distributions show that demagnetization is most pronounced at the PM edges nearest to the stator. The largest demagnetization ratios were 1.45 % in a situation of pure demagnetizing and 0.64 % in a situation typical of usual operation condition.

As a counter to this weakness and to enhance the reliability of the motor, topology optimization used to minimize, or even nullify, demagnetization without compromising high performance. The subsequent section demonstrates the details of the topology optimization method.

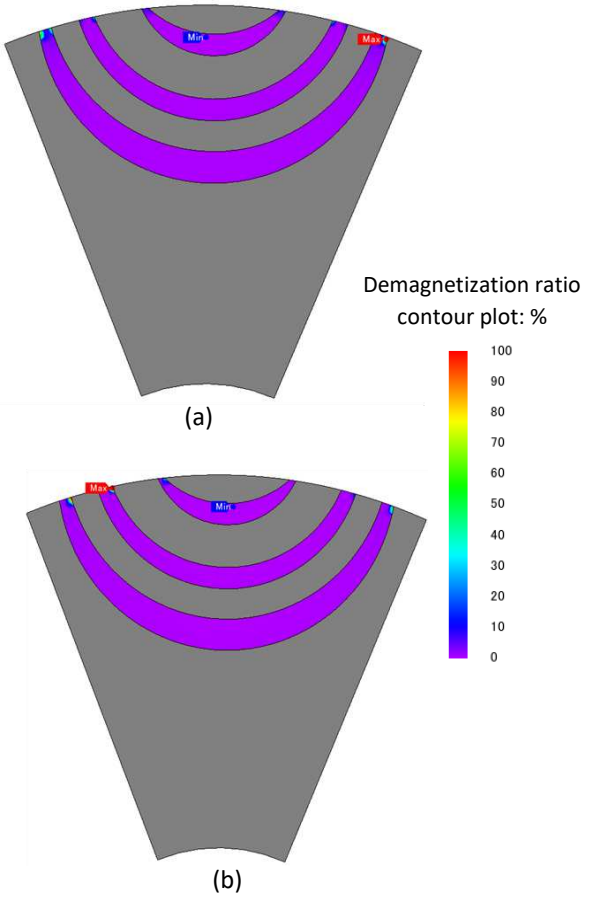


Fig.7. Demagnetization ratio contour plot. a) Pure demagnetizing current. b) Normal operating current.

Topology Optimization

As demonstrated in the demagnetization analysis of the PO optimal design, PM edges closest to the stator were revealed to be most vulnerable, and harsh demagnetization was observed to take place in the initial 2 mm of the rotor surface. To address this issue, topology optimization (TO) was introduced in this region and leveraged its flexibility in material distribution to reveal an optimal distribution SMM and air. In this step, the first 2 mm of the PM surface was recessed and defined as the design domain, in which the TO process aims to redistribute material so that demagnetization is minimized, or even eliminated, while maintaining machine performance.

Topology optimization using NGnet

Topology optimization was performed in this study using the NGnet method, where the distribution of material in the design domain is described by a shape function *y(x)* defined as the weighted sum of normalized Gaussian basis functions G_i:

$$y(\boldsymbol{x}) = \sum_{i=1}^{N} w_i b_i(\boldsymbol{x}), \tag{2}$$

$$b_i(\boldsymbol{x}) = \frac{G_i(\boldsymbol{x})}{\sum_{j=1}^{N} G_j(\boldsymbol{x})}, \tag{3}$$

where N is the total number of Gaussian functions, w_i are the weighting coefficients, and $\mathbf{x}$ is the position vector. Each Gaussian basis is defined by its center position and standard deviation σ. The Gaussian centers and deviations are preset such that they cover the design domain completely, and partial overlap between Gaussian bases is generally recommended, as overlapping Gaussian bases have been shown to provide better quality solutions than no overlap[26].

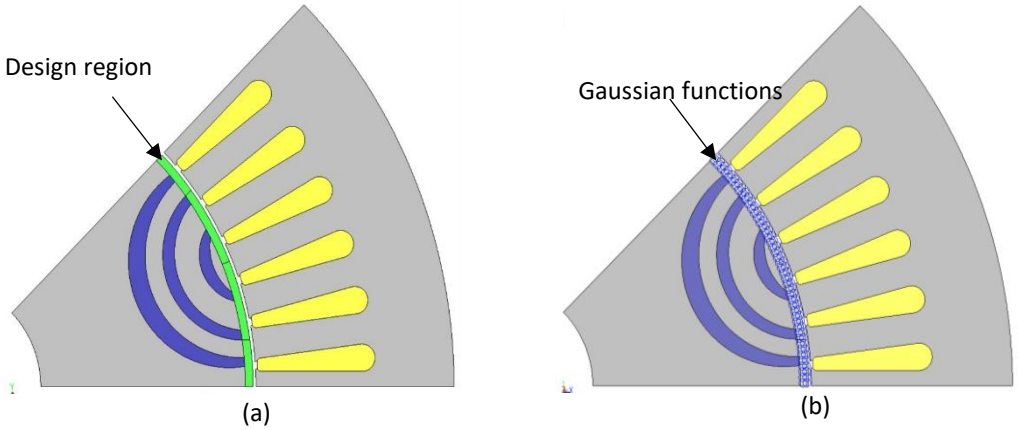


Fig. 8. Motor model used in this study. (a) The design region. (b) Distribution of Gaussian

At optimization, the material type of each FE element is selected from the sign of *y(x)*: If *y(x)* ≥ 0, the element is switched to the "ON" state (e.g., Steel, SMM, or other magnetic material); otherwise, it is set to the "OFF" state (e.g., air, aluminum, or other non-magnetic material). The weights vector $\boldsymbol{w} = \{w_i | \ i = 1, 2, \dots, N\}$ is then optimized using MOGA to achieve the optimization goals while satisfying pre-determined constraints.

The choice of *N* is directly related to both the geometric complexity that can be achieved in the final design and the number of generations required for the solution to obtain a steady state.

This parametric representation possesses a compact and continuous form of the design that will allow the MOGA to effectively search for an optimum SMM and air distribution in the defined design area.

Implementation of NGnet on the parametric optimal 3- Layer IPMSM

NGnet-based TO method is applied to the optimal 3-layer rotor configuration obtained from the preceding PO stage. The objective is to re-design the region most susceptible to demagnetization, identified in the demagnetization analysis as the first 2 mm beneath the rotor surface.

The optimization objectives are to maximize the GD and minimize the torque ripple, subject to the same performance constraints applied in the PO stage. The defined design domain consists of this 2 mm surface layer of the rotor and is divided into two symmetric halves. In order to guarantee a geometrically symmetric and mechanically balanced design, mirror symmetry is enforced.

The design domain is illustrated in Fig. 8, where 90 Gaussian basis functions are placed with a standard deviation of σ = 0.001 m to control the material distribution. In the binary material definition adopted here, an “ON” state corresponds to SMM, and an “OFF” state corresponds to air. To ensure manufacturability, the mesh within the design domain is generated using rectangular elements, while the remainder of the model is discretized with triangular elements. The initial mesh element size in the design domain is set to 1 mm. It is widely known that TO problems are mathematically ill-posed problems and mesh-dependent in terms of geometry due to the non-closed nature of the solution space. In[27] a good review of the numerical instabilities in TO are discussed. The reason for mesh dependencies is that while the mesh is being refined, a better solution can always be found, by incorporating additional involved structures, with progressively greater details. To investigate the impact of mesh refinement in our case, an additional study was conducted with a finer mesh size of 0.25 mm.

Analysis of Topology Optimization Results

The results obtained from the NGnet-based TO are shown in Fig. 9, where the green points represent the full set of evaluated designs, and the blue points denote the Pareto front optimal points in the machine GD–torque ripple space. The optimal design, defined as the best trade-off between objectives, while satisfying the design constraints, is indicated on each plot. Two cases are considered: (a) a design region mesh size of 1 mm and (b) a refined mesh size of 0.25 mm.

The corresponding cross-sectional shapes of the optimal designs are shown in Fig. 10. In addition to the geometry visualization, the finite element mesh for the same optimal designs is shown in Fig. 11, where gray areas denote SMM material and white areas represent air.

As shown in Figs. 10 and 11, by reshaping the rotor surface and incorporating air barriers of both 1 mm and 0.25

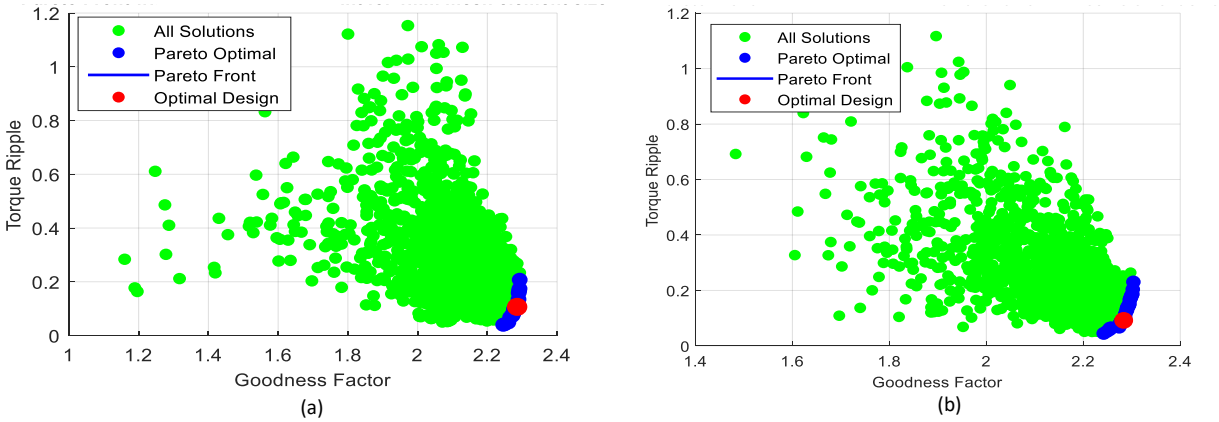


Fig. 9. Pareto fronts and distribution of TO solutions obtained using the NGnet: (a) mesh size in design region = 1 mm, (b) mesh size in design region = 0.25 mm.

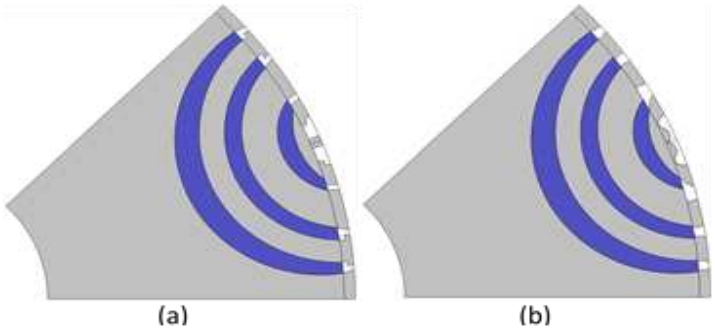


Fig. 10. Cross-sectional geometry of the TO optimal designs for (a) 1 mm mesh size and (b) 0.25 mm mesh size in the design region. (white = air, gray = SMM).

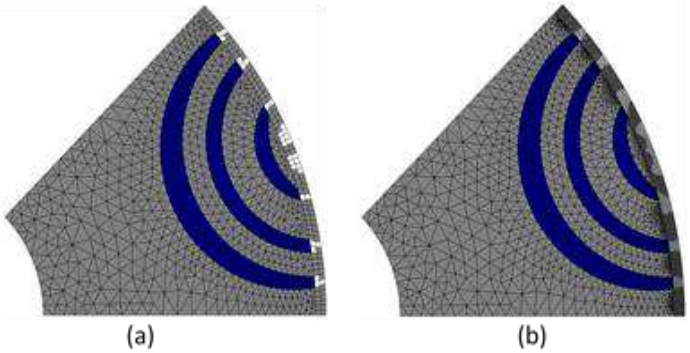


Fig. 11. FE mesh of the TO optimal designs (a) 1 mm mesh size and (b) 0.25 mm mesh size in the design region (white = air, gray = SMM).

mm mesh sizes—wherein the smaller 0.25 mm mesh provided better control over flux distribution and allowed for the creation of more detailed features—TO improved flux guidance and reduced leakage. Because these barriers transition from air to SMM, regions of alternate permeability are created, which create magnetic saliency by generating various reluctance paths along d- and q-axes. This higher saliency raises inductance difference and hence reluctance torque and ensuring that PM flux is more effectively directed to generate maximum PM torque.

To directly compare the influence of mesh refinement, Fig. 12 overlays the Pareto fronts from the 1 mm and 0.25 mm cases on the same plot. The displayed Pareto fronts are obtained through curve fitting of the optimal designs; therefore, some individual optimal design points may not lay exactly on the fitted curve. The initial design from PO, which used as the starting point for TO, is also indicated. The 0.25 mm mesh case appeared to be better overall. Compared to the 3-layer PO optimal design, the 1 mm-mesh TO optimal design increases average torque by about 2.8%. It reduces torque ripple by approximately 45%. It decreases magnet area by around 4.7%. It improves the GD by about 10.4% and raises the power

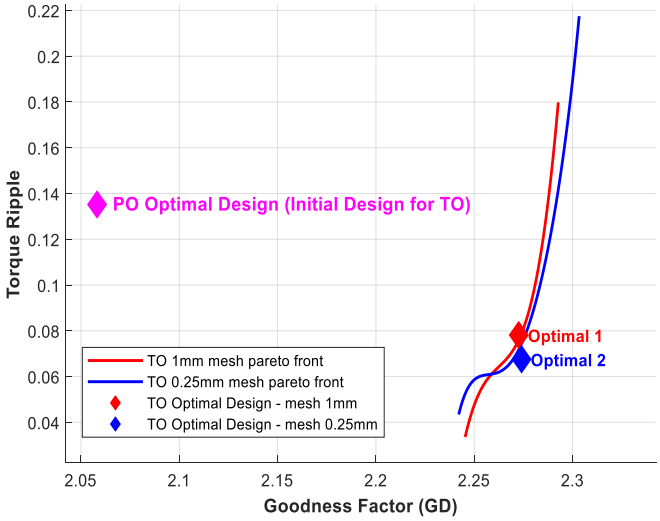


Fig. 12. Comparison of Pareto fronts for TO results obtained with 1 mm and 0.25 mm mesh sizes in the design region, with the PO optimal design indicated.

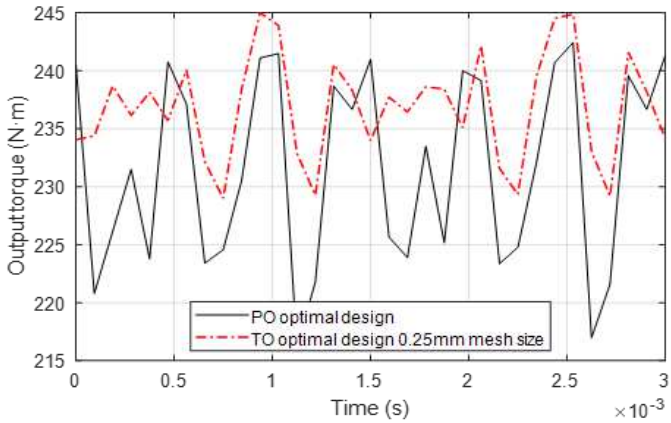


Fig. 13. Output torque waveforms of the PO optimal design and the TO optimal design using 0.25 mm mesh size in the design region.

factor by roughly 12.6%. Similarly, the 0.25 mm-mesh TO optimal design achieves an average torque increase of 3.5%. It has a torque ripple reduction of 50% and a magnet area reduction of 4.7%. It shows a GD improvement of 10.5% and a power factor increase of 13.5%. This demonstrates that TO significantly improves performance compared to the original PO optimal design. Fig. 13 compares the torque waveforms of the PO optimal design and the TO optimal design with 0.25 mm mesh size in the design region. It is evident that TO reduces torque ripple significantly while slightly increasing the average torque compared with the PO design.

Table 4 also provides a quantitative comparison of the best designs for 1 mm, 0.25 mm, and PO optimal design. The 0.25 mm mesh design is better than the 1 mm mesh design, as the PO optimum design, in all the performance measures.

Performance Metric	3- Layer PO optimal design	1 mm mesh TO optimal design	0.25mm mesh TO optimal design
Average Torque [Nm]	228.85	235.28	236.89
Torque ripple percentage	13.52%	7.38%	6.75%
Magnet Area [mm^2]	438.93	418.42	418.42
Goodness factor	2.0582	2.2719	2.274
Power Factor	0.5505	0.6197	0.6246

Table 4. Comparison of optimal design obtained from PO and TO with 1 mm and 0.25 mm mesh sizes in the design region.

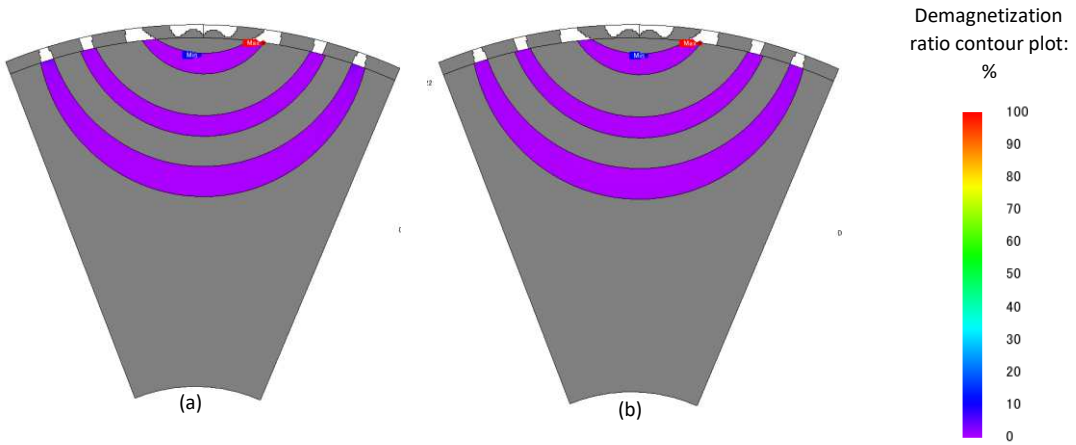


Fig. 14. Demagnetization ratio contour plot. a) Pure demagnetizing current. b) Normal operating current.

Since the 0.25 mm mesh demonstrated superior electromagnetic performance, a demagnetization analysis was carried out for the TO optimal design using this mesh size, under the same operating conditions and with the same procedure described in the PO demagnetization section. The demagnetization ratio at the normal operating phase current angle was 0.39%, and under pure demagnetizing current it was 0.58%. When comparing the PO optimal design, the TO rotor with a 0.25 mm mesh showed a much lower demagnetization ratio, indicating reduced risk of irreversible PM flux loss. As shown in Fig.14, the TO optimal design demagnetization ratio contour plot exhibits a much lower demagnetization ratio compared to the PO optimal design, justifying the enhanced robustness of the PMs against both normal and severe current. This improvement is obtained by trimming the previously vulnerable 2 mm PM section identified in the PO optimal design and redistributing SMM and air at the rotor surface, leading to enhanced PM utilization and overall motor performance.

Conclusion

This paper successfully applied a two-step optimization methodology to enhance the performance of an additively manufactured layered IPMSM. Combining topology and parametric optimization is an effective method to explore the design space associated with the alternating PM and SMM layers. The optimized rotor provided better electromagnetic performance and improved PM material usage and reduced the risk of demagnetization. For researchers seeking to enhance the design of high-performance electric motors, this paper offers a clear and reproducible methodology by detailing each step.

Data availability

The datasets used and/or analysed during the current study available from the corresponding author on reasonable request.

References

1. Niu, L. Optimization design and torque performance research of interior permanent magnet synchronous motors. Sci. Rep. 15, 8822, https://doi.org/10.1038/s41598-025-93285-x (2025).

2. Niu, L. & Zhang, M. The optimal design and research of interior permanent magnet synchronous motors for electric vehicle applications. J. Eng. 1–20, https://doi.org/10.1049/tje2.12258 (2023).
3. Vlachou, V. I., Sakkas, G. K., Xintaropoulos, F. P., Pechlivanidou, M. S. C., Kefalas, T. D., Tsili, M. A. & Kladas, A. G. Overview on permanent magnet motor trends and developments. Energies 17 (2), 538, https://doi.org/10.3390/en17020538 (2024).
4. Kolehmainen, J. Dovetail rotor poles in synchronous permanent magnet and reluctance machines. PhD dissertation, Aalto Univ., Finland (2011).
5. Ibrahim, M., Bernier, F. & Lamarre, J.-M. Novel multi-layer design and additive manufacturing fabrication of a high power density and efficiency interior PM motor. In Proc. IEEE Energy Convers. Congr. Expo. (ECCE), Detroit, MI, USA (2020).
6. Ibrahim, M., Bernier, F. & Lamarre, J.-M. Design of a PM-assisted synchronous reluctance motor utilizing additive manufacturing of magnetic materials. In Proc. IEEE Energy Convers. Congr. Expo. (ECCE), Baltimore, MD, USA (2019).
7. Selema, A., Ibrahim, M. N. & Sergeant, P. Metal additive manufacturing for electrical machines: Technology review and latest advancements. Energies 15 (3), 1076, https://doi.org/10.3390/en15031076 (2022).
8. Thabuis, A., Ren, X. & Perriard, Y. Enhanced electric motors using multi-functional 3D printed winding with integrated heat sinks. IEEE Trans. Energy Convers. 38 (2), 849–858, https://doi.org/10.1109/TEC.2022.3221189 (2023).
9. Naseer, M. U., Kallaste, A., Asad, B., Vaimann, T. & Rassõlkin, A. A review on additive manufacturing possibilities for electrical machines. Energies 14 (7), 1940, https://doi.org/10.3390/en14071940 (2021).
10. Wrobel, R. & Mecrow, B. A comprehensive review of additive manufacturing in construction of electrical machines. IEEE Trans. Energy Convers. 35 (2), 1054–1064, https://doi.org/10.1109/TEC.2020.2964942 (2020).
11. Vaz, R. F., Garfias, A., Albaladejo, V., Sanchez, J. & Cano, I. G. A review of advances in cold spray additive manufacturing. Coatings 13 (2), 267, https://doi.org/10.3390/coatings13020267 (2023).
12. Chen, H. & Lee, C. H. T. Parametric sensitivity analysis and design optimization of an interior permanent magnet synchronous motor. IEEE Access 7, 159918–159929, https://doi.org/10.1109/ACCESS.2019.2950773 (2019).
13. Chu, G., Pouramin, A., Dutta, R., Rahman, M. F., Lovatt, H. & Sarlioglu, B. A new mechanical-strength-oriented rotor parametric model design for the optimization of a very-high-speed IPMSM. In Proc. IEEE Energy Convers. Congr. Expo. (ECCE), 6092–6097, https://doi.org/10.1109/ECCE.2019.8912980 (2019).
14. Park, J.-C., Kim, J.-H., Park, S.-H., Kim, K.-O., Sung, M.-H. & Lim, M.-S. Design optimization using asymmetric rotor in IPMSM for torque ripple reduction considering forward and reverse directions. IEEE Trans. Magn. 59 (11), 1–5, https://doi.org/10.1109/TMAG.2023.3292295 (2023).
15. Gadiyar, N. & Wang, B. Topology optimization of electric machines: A review. In Proc. IEEE Energy Convers. Congr. Expo. (ECCE), 1–8, https://doi.org/10.1109/ECCE50734.2022.9948073 (2022).
16. Lee, C. & Jang, I. G. Topology optimization of the IPMSMs considering both the MTPA and FW controls under the voltage and current limitations. IEEE Trans. Ind. Electron. 70 (8), 8244–8253, https://doi.org/10.1109/TIE.2023.3234136 (2023).
17. Hayes, A. C., Träff, E. A., Sørensen, C. V., Willems, S. V., Aage, N., Sigmund, O. & Whiting, G. L. Topology optimization for structural mass reduction of direct drive electric machines. Sustain. Energy Technol. Assess. 57, 103254, https://doi.org/10.1016/j.seta.2023.103254 (2023).
18. Lamarre, J.-M. & Bernier, F. Permanent magnets produced by cold spray additive manufacturing for electric engines. J. Therm. Spray Technol. 28, 1709–1717, https://doi.org/10.1007/s11666-019-00917-6 (2019).
19. Bernier, F., Ibrahim, M., Mihai, M., Thomas, Y. & Lamarre, J.-M. Additive manufacturing of soft and hard magnetic materials used in electrical machines. Metal Powder Rep. 75 (6), 334–343, https://doi.org/10.1016/j.mprp.2019.12.002 (2020).
20. JSOL Corporation. JMAG-Designer Version 24.0 Reference Manual. Tokyo, Japan (2025).
21. Duan & Ionel, D. M. A review of recent developments in electrical machine design optimization methods with a permanent-magnet synchronous motor benchmark study. IEEE Trans. Ind. Appl. 49 (3), 1268–1275, https://doi.org/10.1109/TIA.2013.2252597 (2013).
22. Badewa, O. A., Mohammadi, A., Lewis, D. D., Ionel, D. M., Essakiappan, S. & Manjrekar, M. Optimization of an electric vehicle traction motor with a PM flux intensifying stator and a reluctance outer rotor. In Proc. IEEE Transp. Electrific. Conf. Expo. (ITEC), 1–6, https://doi.org/10.1109/ITEC55900.2023.10186958 (2023).
23. Badewa, O. A., Mohammadi, A., Ionel, D. M., Essakiappan, S. & Manjrekar, M. Electric vehicle traction motor with a reluctance outer rotor and a modular stator with AC concentrated toroidal windings and PM or DC wave winding

excitation. In Proc. IEEE Energy Convers. Congr. Expo. (ECCE), 3845–3850, https://doi.org/10.1109/ECCE53617.2023.10362185 (2023).
24. Xia, B., Fei, W., Luk, P. C. K. & Wu, D. Design of a multi-layer interior ferrite permanent magnet synchronous machine for traction applications. In Proc. 7th IET Int. Conf. Power Electron. Mach. Drives (PEMD), 1–6, https://doi.org/10.1049/cp.2014.0444 (2014).
25. Bernier, F., Lamarre, J.-M., Hirayama, Y. & Takagi, K. Anisotropic magnets fabricated by cold spray additive manufacturing. J. Jpn. Soc. Powder Powder Metallurgy 72, S219–S226, https://doi.org/10.2497/jjspm.14E-T16-05 (2025).
26. Sato, S., Sato, T. & Igarashi, H. Topology optimization of synchronous reluctance motor using normalized Gaussian network. IEEE Trans. Magn. 51 (3), Art. no. 8200904, https://doi.org/10.1109/TMAG.2014.2359679 (2015).
27. Sigmund, O. & Petersson, J. Numerical instabilities in topology optimization: A survey on procedures dealing with checkerboards, mesh-dependencies and local minima. Struct. Optim. 16, 68–75, https://doi.org/10.1007/BF01214002 (1998).

Funding

This research was funded by the National research Council of Canada (NRC)

Open access funding provided by The Science, Technology & Innovation Funding Authority (STDF) in cooperation with The Egyptian Knowledge Bank (EKB).

Author contributions statement

All authors have contributed equally in this work.